

Diffuse scattering as an indicator for martensitic variant selection

Lei Gao^a, Xiangdong Ding^{a,b,*}, Hongxiang Zong^a, Turab Lookman^{b,*}, Jun Sun^a,
Xiaobing Ren^{a,c}, Avadh Saxena^b

^a State Key Laboratory for Mechanical Behavior of Materials, Xi'an Jiaotong University, Xi'an 710049, China

^b Theoretical Division, Los Alamos National Laboratory, Los Alamos, NM 87545, USA

^c Ferroic Physics Group, National Institute for Materials Science, Tsukuba, 305-0047 Ibaraki, Japan

Received 9 October 2013; received in revised form 25 November 2013; accepted 25 November 2013

Abstract

Diffuse scattering is an important precursor phenomenon prior to the martensitic transformation (MT). It is related to the correlated atomic position fluctuations prior to the MT and can provide important hints of the transformation mechanism. However, the role of this precursor phenomenon in the MT is not clear so far. Here we study the evolution of diffraction patterns prior to temperature- and stress-induced MTs and consider the evolution of atomic configurations during the whole MT process, using molecular dynamics simulations on a generic body-centered cubic–hexagonal close-packed transformation as an example. Our results show that, although the diffuse scattering changes with external fields, there exists a general relationship between the transformation pathways, the diffuse scattering streaks and the martensitic products. Two preferred transformation pathways with opposite shuffle directions lead to a single specific diffuse scattering streak prior to the MT and form one pair of anti-variants after the MT. Thus the distribution of diffuse scattering acts as an indicator of the selection of martensitic variants. In addition, we find that the applied stress can change the shear order parameter of the phase transformation, and subsequently determines the preferred transformation pathways and the distribution of diffuse scattering streaks. This work establishes a relationship between the transformation mechanism, the precursor phenomenon and the products after the MT under the influence of external fields.

© 2013 Acta Materialia Inc. Published by Elsevier Ltd. All rights reserved.

Keywords: Precursor phenomena; Martensitic transformation; Diffuse scattering; Molecular dynamics simulations

1. Introduction

The martensitic transformation (MT) is a structural, first-order and diffusionless phase transformation in which an open structure at high temperature usually transforms into a close-packed structure at low temperature. The martensitic transformation in steel represents the most economically important example of this kind of phase transformation, and its increasing applications in functional materials, such as shape memory alloys, have attracted significant attention for decades.

One of the most interesting features of martensitic transformations is the ubiquitous precursor phenomenon [1–3], a signature of the impending instability of the system towards a martensitic phase. Prior to a temperature-induced MT, several important precursor phenomena have been observed as the temperature approaches the transformation temperature [1–15]; for example, most of body-centered cubic (bcc) martensitic materials exhibit a low-lying TA_2 phonon branch [4–6] and elastic constant $C' = (C_{11} - C_{12})/2$ softening [7–9] when approaching the transformation temperature. A number of TEM observations have reported diffuse scattering along the $\langle 110 \rangle^*$ directions [10–15]. In TiNiFe alloys, the diffuse scattering is found to correspond to tiny “domains” [11,12], rather than the tweed structure as observed in NiAl alloys [5,15]. These precursor phenomena play a significant role in the kinetics

* Corresponding authors.

E-mail addresses: dingxd@mail.xjtu.edu.cn (X. Ding), txl@lanl.gov (T. Lookman).

of martensitic transformation, and provide crucial clues to understanding the transformation mechanism. However, the relationship between these precursor phenomena and the products after the MT is still not clear.

Stress can also induce a martensitic transformation. It is known that C' softening also exists prior to a stress-induced MT [16–18], and the C' softening behavior depends on the applied stress, in contrast to the temperature-induced MT, where the softening occurs in all three equivalent directions. These results suggest that the precursor behavior prior to a stress-induced MT differs from the well-known behavior prior to a temperature-induced MT. Nevertheless, it is still not clear whether other precursor phenomena exist prior to a stress-induced MT, and how they differ from that in the temperature-induced MT. In addition, the relationship between the precursor phenomena and the transformation products under stress is also not clear. The diffuse scattering intensity distribution is rich in information on structural disorder and provides an appropriate diagnostic tool for us to study the correlated atomic position fluctuations in the precursor state and reveal its role in the MT. Thus, the purpose of this work is to use molecular dynamics (MD) simulations to investigate the diffuse scattering phenomena prior to the MTs under different external fields (both temperature and stress) and to establish the relationship between the diffuse scattering prior to the MT and the products after the MT.

Using a general bcc–hexagonal close-packed (hcp) phase transformation as example, we study here the evolution of diffraction patterns prior to temperature- and uniaxial stress-induced MTs via MD simulations. Our results show that, unlike diffuse scattering prior to a temperature-induced MT, the intensity of diffuse scattering under external stress increases only along certain specific directions, while it decreases along the others. Through analysis of the atomic evolutions and pathways of phase transformation during the stress- and temperature-induced MTs, we find that there is a general relationship between the diffuse scattering precursor phenomenon, the transformation pathways and the transformation products. Two preferred transformation pathways with opposite shuffle directions lead to a single specific diffuse scattering streak prior to the MT and form one pair of anti-variants after the MT. In addition, the applied stress can change the shear order parameter of the phase transformation, and then determines the preferred transformation pathways and the distributions of diffuse scattering. The understanding gleaned from this work enables us to establish a relationship between the transformation mechanism, the increase in diffuse scattering prior to the MT and the products after the MT under external fields.

2. Simulation and calculation methods

We used the embedded atom method potentials developed by Mendelev and Ackland [19] as the input for MD simulations. This potential reproduces properties such as

the cohesive energy, elastic constants, and especially the MT between bcc and hcp very well. Although the potential was developed for pure Zr, we do not expect that such a semi-empirical potential could reproduce all of the phase transformation properties of Zr exactly (e.g. the bcc to hcp transition temperature reproduced by this potential under periodic boundary conditions (192.4 K) is significantly lower than the experimental value of 1135 K [20]). The reasons for the focus on a general bcc to hcp phase transformation are: (i) it is a martensitic transformation with coupling of shuffle (primary-order parameter) and shear (secondary-order parameter), which occurs in most martensitic alloys [2]; and (ii) the transformation follows the Burgers mechanism [21]. Such a well-known phase transformation allows us to detect how the interaction between the transformation mechanism and the external fields (e.g. temperature and applied stress) affects the diffuse scattering prior to the MT and the products after the MT.

In our calculations we adopted the isothermal–isobaric ensemble, in which a Nosé–Hoover thermostat was used to control the temperature and a Parrinello–Rahman barostat was used to control the pressure. The initial MD cell (with a bcc structure) has dimensions of $50a \times 50a \times 50a$, where a is the lattice constant of the bcc structure at 0 K. To avoid the existence of free surfaces, periodic boundary conditions in three dimensions were used for all the MD simulations. The MD calculations were carried out using the LAMMPS code [22] and the atomic configurations were displayed using ATOMEYE [23].

We first started the MD simulations on a temperature-induced MT. The ensemble was first relaxed at 400 K for 100 ps to make sure that the system reached the equilibrium state. The ensemble was then cooled from 400 to 150 K at a cooling rate of 0.1 K ps^{-1} . During the cooling process we monitored the changes in MD cell axis lengths as a function of temperature. The results are shown in Fig. 1a. From this figure we obtained a bcc–hcp transformation starting temperature (M_s) of 192.4 K, which is much lower than the experimental one for pure Zr (1135 K). This means that the MT reproduced by this potential is not the same as that for real Zr; we should consider the potential to be that for a model bcc to hcp transformation. However, we note that the understanding obtained from this model material should also be valid for the bcc to hcp transformation of real Zr, as the bcc to hcp transformations in the two systems follow the same mechanism (the Burgers mechanism). Although the higher transformation temperature enhances the strength of thermal fluctuations, it does not alter the transformation mechanism. In addition, previous experimental results show the existence of diffuse scattering prior to temperature-induced bcc to hcp transformation at 1273 K [24], similar to the results obtained from the present MD simulations at low temperature.

Knowing the transformation temperature of the ensemble, we then simulated the stress-induced MT. Initially, the

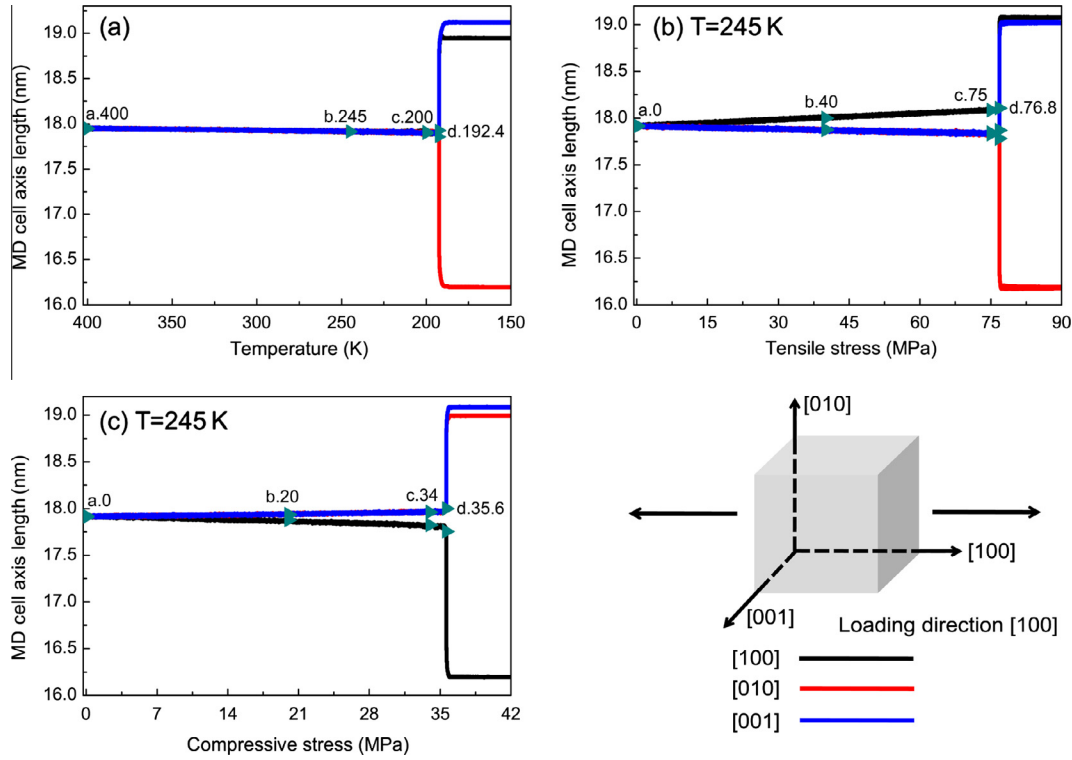


Fig. 1. The MD cell axis length changes as functions of temperature and stress, allowing the martensitic transformation to be determined. (a) The MD cell axis length as a function of temperature for temperature-induced martensitic transformation (cooling process); the martensite start temperature, M_s is 192.4 K; (b, c) MD cell axis length vs. stress curves for [100] uniaxial tensile stress- and compressive stress-induced martensitic transformations, respectively. The critical stresses for [100] uniaxial tensile stress and compressive stress-induced martensitic transformation are 76.8 and 35.6 MPa, respectively.

temperature of the ensemble was reduced from 400 to 245 K (above M_s) at a cooling rate of 0.1 K ps^{-1} . The ensemble was then held for 100 ps to establish equilibrium, before an external stress was applied. Initially, a uniaxial tensile stress was applied along the [100] direction, with a loading rate of 0.1 MPa ps^{-1} . The variation in cell size with external stress is shown in Fig. 1b. We note that the critical stress (σ_c) for a uniaxial tensile stress-induced MT is 76.8 MPa. Using the same procedure, we also applied a uniaxial compressive stress along the [100] direction at 245 K. From Fig. 1c we note that the critical stress (σ_c) for uniaxial compressive stress-induced MT is 35.6 MPa.

To study the diffuse scattering phenomena prior to both temperature- and stress-induced MTs, we output the atomic configurations every 0.1 K during the cooling process for the temperature-induced MT and every 0.1 MPa for the uniaxial stress-induced MTs. These output configurations were further relaxed by energy minimization to reduce the thermal vibration, and the corresponding diffraction patterns were then calculated using the formula [25]

$$I(\mathbf{k}) = \sum_n f \exp(-i\mathbf{k} \cdot \mathbf{r}_n), \quad (1)$$

where $|I|^2$ is the diffracted intensity, f is the scattering factor of Zr, \mathbf{k} is the wave vector and \mathbf{r}_n is the position of atom n . The scattering factor of Zr has been taken as 1, as it has no

influence on the tendency of the crystal for diffuse scattering. The summation was performed over all of the atoms in the ensemble. To ensure that the minimization of energy leading to new atomic positions did not change the diffuse scattering due to the phase transformation, we maintained the same maximum diffracted intensity of the system before and after energy minimization. However, we eliminated the diffraction intensities caused by thermal vibration (which are the disordered points from the main streaks of the diffraction pattern before the energy relaxation; their intensities are near the minima among the diffraction intensities before the energy relaxation).

3. Results

3.1. Distribution of diffuse scattering prior to temperature- and stress-induced martensitic transformations

The calculated diffraction patterns along the $[1\bar{1}\bar{1}]$ zone axis, prior to the temperature-induced MT, are shown in Fig. 2a–d. The temperatures in Fig. 2a, b, c and d correspond to the marked points in Fig. 1a. Except for the diffuse streaks, all the sharp reflections in these figures can be indexed as bcc structure. The most interesting features of these diffraction patterns are the complex diffuse streaks, which are unexpected for ideal bcc structure. In

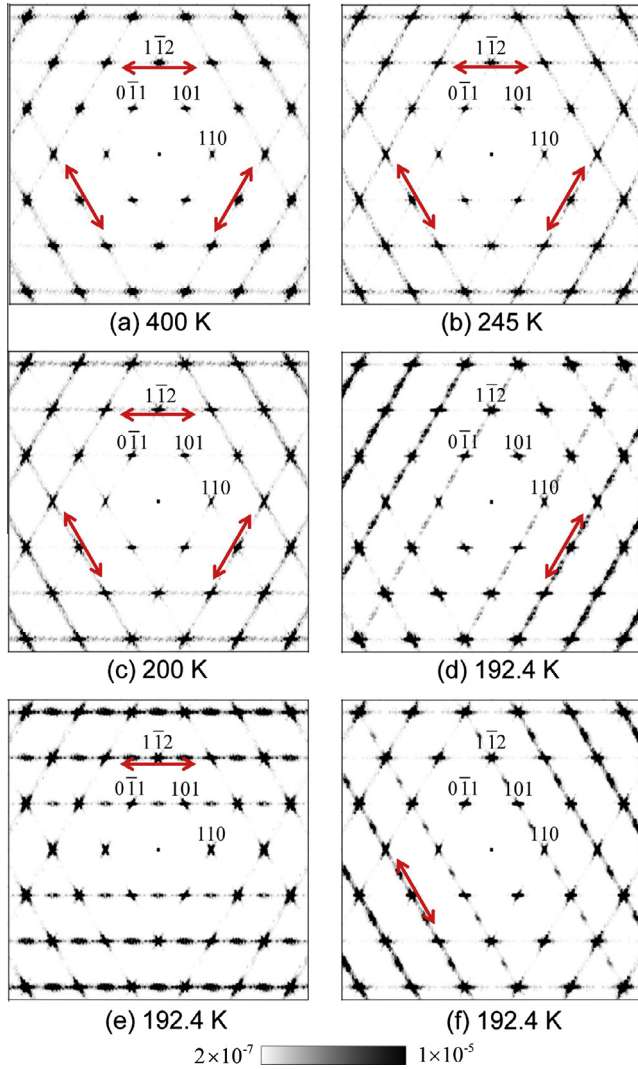


Fig. 2. The change in diffraction patterns along the $[1\bar{1}\bar{1}]$ zone axis with temperature prior to a temperature-induced MT. Shown are three enhanced diffuse scattering streaks along the $[1\bar{1}\bar{1}]$ zone axis prior to a temperature-induced MT. The temperatures at (a)–(d) correspond to the points marked in Fig. 1a. The diffuse scattering patterns in (a)–(c) all include three diffuse streaks along the $[110]^*$, $[101]^*$ and $[0\bar{1}1]^*$ directions, as shown by the red arrows. When the temperature is further cooled to M_s , only the diffuse scattering streak along the $[101]^*$ direction (d) is found to survive. The diffuse scattering streaks along the $[110]^*$ (e) and $[0\bar{1}1]^*$ (f) directions can also be found if the cooling process is repeated. The probabilities of finding (d), (e) and (f) at M_s are the same. (For interpretation of the references to color in this figure legend, the reader is referred to the web version of this article.)

the following, “ $[lmn]$ ” and “ $\langle lm n \rangle$ ” stand for a specific direction lmn and a group of crystallographically equivalent directions lmn in real space, respectively, and those with “ $*$ ” represent the same in reciprocal space. As the temperature of the ensemble decreases from 400 to 200 K (Fig. 2a–c), diffuse streaks can be observed along three of the crystallographically equivalent $\langle 110 \rangle^*$ directions ($[110]^*$, $[101]^*$ and $[0\bar{1}1]^*$, as shown by the arrows in Fig. 2) and the intensity of the diffuse streaks increases gradually with decreasing temperature. Hereon we use

the notation $[110]^*$ to represent the diffuse scattering along both the $[110]^*$ and $[\bar{1}\bar{1}0]^*$ directions, as these directions arise from the two shuffles in the same $(1\bar{1}0)$ plane. The same meaning applies to the other $\langle 110 \rangle^*$ directions.

When the temperature of the ensemble is further cooled to M_s (192.4 K), we find that only the intensity of the diffuse streak along the $[101]^*$ direction is further enhanced, whereas the other two directions in Fig. 2a–c ($[110]^*$ and $[0\bar{1}1]^*$) become weak (Fig. 2d). To understand the reason for this phenomenon, we repeated the cooling process 30 times and calculated the probability of getting a given diffuse scattering at 192.4 K. The statistical results show that repetition of the cooling process also leads to an increase in diffuse scattering intensity along the $[110]^*$ (Fig. 2e) or $[0\bar{1}1]^*$ (Fig. 2f) direction, and the probability of finding an increase in diffuse scattering intensity along $[101]^*$, $[110]^*$ and $[0\bar{1}1]^*$ is actually the same. Thus, we can attribute this phenomenon to the limitation of our MD cell size. When the temperature is fairly close to M_s , only one of the three equivalent diffuse scattering directions is randomly selected, and this becomes the dominant one under further cooling.

Interestingly, we find that the diffuse scattering along the $[101]^*$ and $[10\bar{1}]^*$ directions is conjugate. If the diffuse streak along the $[101]^*$ direction increases (Fig. 2d) as viewed from the $[1\bar{1}\bar{1}]$ zone axis, the diffuse streak along the $[10\bar{1}]^*$ direction is also enhanced, as shown as Fig. 3. Similarly, we find that the $[110]^*$ and $[1\bar{1}0]^*$ directions and the $[0\bar{1}1]^*$ and $[011]^*$ directions are also conjugate. The reasons for this conjugate relationship will be discussed in Section 4.2. From the observations in Figs. 2 and 3, we can conclude that the increase in diffuse scattering intensity can be found in all six equivalent $\langle 110 \rangle^*$ directions prior to the temperature-induced MT.

The calculated diffraction patterns along the $[1\bar{1}\bar{1}]$ zone axis prior to the $[100]$ uniaxial tensile stress-induced MT are shown as Fig. 4a–c. The initial state (without external stress) is the same as Fig. 2b, in which the streak intensity along the $[110]^*$, $[101]^*$ and $[0\bar{1}1]^*$ directions is equal. However, upon loading, the streak intensity becomes

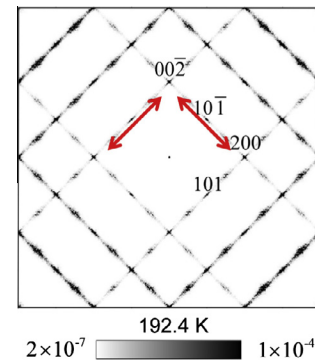


Fig. 3. The calculated diffraction pattern viewed from the $[010]$ zone axis for the case that the diffuse streak along the $[101]^*$ direction survives viewed from the $[1\bar{1}\bar{1}]$ zone axis at M_s . The diffuse streaks along the $[101]^*$ and $[10\bar{1}]^*$ directions are conjugate to each other.

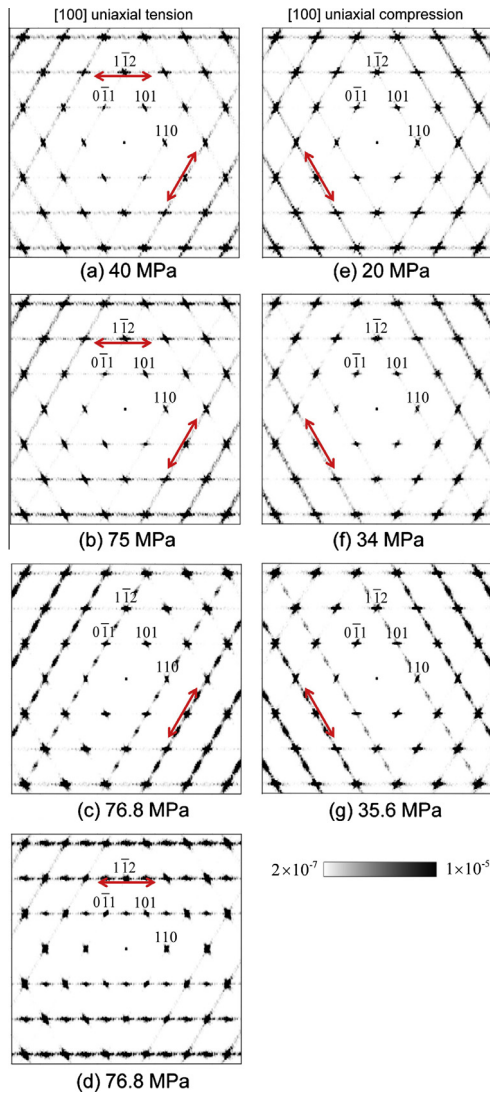


Fig. 4. Using the $[1\bar{1}\bar{1}]$ zone axis, the change of diffuse scattering patterns with stress prior to [100] uniaxial tensile stress- and compressive stress-induced MTs. There are two enhanced diffuse scattering streaks prior to the [100] uniaxial tensile stress-induced MT, whereas there is only one enhanced diffuse scattering streak in this zone axis prior to the [100] uniaxial compressive stress-induced MT. The left panel of this figure (a–d) shows the results under [100] uniaxial tensile stress; the right panel of this figure (e–g) shows the results under [100] compressive stress. The initial state (without external stress) is the same as Fig. 2b. Under [100] uniaxial tension, we observe that the two diffuse scattering streaks along both the $[110]^*$ and $[101]^*$ directions become dominant when the [100] uniaxial tensile stress is less than 75 MPa (as shown by red arrows in (a) and (b)). At the critical stress, σ_c (76.8 MPa), at which the uniaxial tensile stress-induced MT occurs, only the diffuse scattering streak along the $[101]^*$ direction becomes dominant for the present tension process (as shown by the red arrow in (c)). A diffuse scattering streak along the $[110]^*$ direction (d) can also be found if the [100] tension process is repeated. The probabilities of finding (c) and (d) at the critical stress are the same. Under the [100] uniaxial compression, we observe that the diffuse scattering streak along the $[0\bar{1}1]^*$ direction is dominant throughout the whole process (as shown by red arrows in (e)–(g)), and the diffuse streaks along both the $[110]^*$ and $[101]^*$ directions decrease. (For interpretation of the references to color in this figure legend, the reader is referred to the web version of this article.)

different along the three equivalent directions. With the [100] uniaxial tensile stress increasing to 40 MPa (Fig. 4a) and even to 75 MPa (Fig. 4b), the diffuse streak intensity along $[110]^*$ and $[101]^*$ strengthens, while the intensity along $[0\bar{1}1]^*$ weakens. When the stress is 76.8 MPa (i.e. the critical stress to induce the MT), only one diffuse scattering (along $[101]^*$) is enhanced (Fig. 4c). The reason for this is the same as for the temperature-induced MT, i.e. the limited MD cell size. If we repeat the [100] uniaxial tension simulations on this ensemble 30 times, we also find that $[110]^*$ (Fig. 4d) is enhanced near the critical stress, and the probability of finding the dominant diffuse scattering along $[110]^*$ and $[101]^*$ is the same. Considering the conjugate relationships between $[110]^*$ and $[1\bar{1}0]^*$ and between $[101]^*$ and $[10\bar{1}]^*$, the above results indicate that, prior to the [100] uniaxial tension-induced MT, the diffuse scattering intensity only increases along four of the six equivalent $\langle 110 \rangle^*$ directions, and decreases along the other two.

The calculated diffraction patterns along the $[1\bar{1}\bar{1}]$ zone axis prior to the [100] compressive stress-induced MT are also shown as Fig. 4e–g. We find that the situation under uniaxial compression is totally opposite to that under uniaxial tension. With the increase in [100] compressive stress to 20 MPa (Fig. 4e) and even to 34 MPa (Fig. 4f), we observe that the diffuse streak intensity along the $[0\bar{1}1]^*$ direction is enhanced, whereas those along both the $[110]^*$ and $[101]^*$ directions are simultaneously weakened. When the stress reaches 35.6 MPa (i.e. the critical stress to induce the MT), the intensity along the $[0\bar{1}1]^*$ direction is further enhanced (Fig. 4g). Repeated runs on the ensemble show that the increase in the diffuse streak occurs only along the $[0\bar{1}1]^*$ direction. As the diffuse scattering along the $[0\bar{1}1]^*$ and $[01\bar{1}]^*$ directions is conjugate, it implies that the increase in diffuse scattering intensity can only be found along two of the six equivalent $\langle 110 \rangle^*$ directions.

In summary, the above results show that the increase in diffuse scattering intensity also occurs prior to stress-induced MT. However, unlike the increase in diffuse scattering intensity in all six equivalent $\langle 110 \rangle^*$ directions prior to a temperature-induced MT, the diffuse scattering prior to a stress-induced MT is closely related to the direction of the external stress.

3.2. Atomistic evolution during temperature- and stress-induced martensitic transformations

To understand the corresponding atomic processes underlying the strengthening and weakening of diffuse scattering prior to these phase transformations, and their relationship to the product of MT, we consider the nature of the atomic configurations during the whole process associated with temperature- and stress-induced MTs.

The bcc–hcp phase transformation is one of the most commonly encountered reconstructive transformations in

crystals of elements in which both shuffle (along $\{110\}$ $\langle 1\bar{1}0 \rangle_{\text{bcc}}$) and shear (along $\{112\}\langle 11\bar{1} \rangle_{\text{bcc}}$) distortions are involved. However, the shuffle or coordinated displacement of atoms is the dominant distortion and has a direct bearing on diffuse scattering. Thus, monitoring the atomic evolution in $\{110\}$ planes, which includes the information on atomic displacements along $\langle 1\bar{1}0 \rangle$ directions, will provide direct evidence for understanding the relationship between diffuse scattering and the result (product phase) of the MT under different external fields (e.g. temperature and different modes of applied stress).

In the temperature-induced MT, our results show that the increase in diffuse scattering intensity can occur along all six equivalent $\langle 110 \rangle^*$ directions. As the $\langle 110 \rangle^*$ streaks have been explained by the occurrence of $\langle 110 \rangle$ transverse displacive waves [26] (for example, the diffuse streak along $[101]^*$ direction corresponds to the $[10\bar{1}]$ transverse displacive wave with $[101]$ polarization), the $(10\bar{1})$ plane is the most suitable plane on which to monitor the reflections of the diffuse streak along the $[101]^*$ direction on the atomic displacements. Fig. 5a–e shows the corresponding

atomic evolution in the $(10\bar{1})$ plane for the cooling process, the diffraction patterns for which are shown in Fig. 2b–d. When the temperature of the ensemble decreases from 400 to 200 K, the atomic configurations in the $(10\bar{1})$ plane (Fig. 5a and b) show that the average structures are still bcc (blue color), except certain atoms (green color) which have a structure between bcc and hcp (orange color). These green atoms are in a distorted bcc structure that is evolving towards the hcp structure. We note that these distorted bcc regions are not stable: they fluctuate from one temperature to another. Further analysis shows that the number of green atoms and their $[101]$ shuffle displacement increase with decreasing temperature. Such phenomena can be seen in all six equivalent $\{110\}$ planes.

When the temperature has dropped to M_s , the diffuse scattering along $[101]^*$ and $[10\bar{1}]^*$ becomes dominant for this cooling process (shown in Fig. 2d and Fig. 3), we can observe that the distorted bcc structure grows rather quickly in the $(10\bar{1})$ plane, and some hcp nuclei (as shown by the arrow in Fig. 5c) are generated from the distorted bcc structure. When the temperature is 0.1 K below M_s

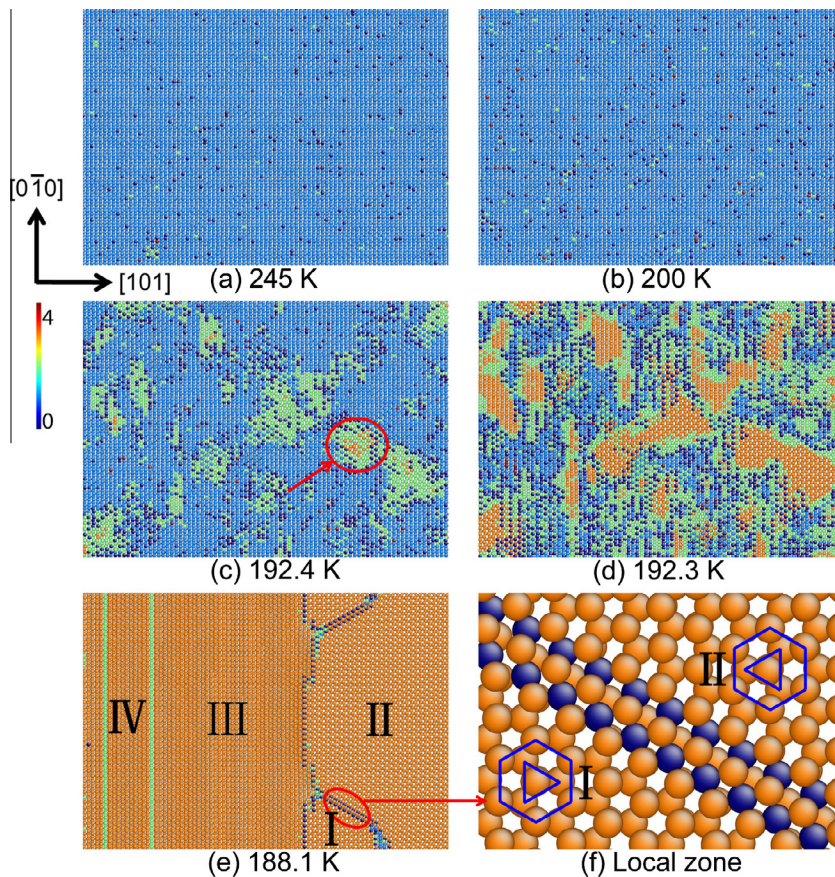


Fig. 5. Evolution of atomic configurations in the $(10\bar{1})$ plane prior to and during the whole process of temperature-induced MT. The dominant diffuse scattering streaks are along the $[101]^*$ and $[10\bar{1}]^*$ directions at M_s for the present cooling process. (a)–(c) correspond to the marked points (b)–(d) in Fig. 1a, as well as the diffraction patterns in Fig. 2(b)–(d); (d) represents the atomic structure during the growing process (at 192.3 K) and (e) represents the product after martensitic transformation (at 188.1 K). The resulting product after the martensitic transformation consists of four types of hcp variants, variants I and II of which are hcp anti-variants with $[0001]$ orientation and variants III and IV are hcp anti-variants with $[11\bar{2}0]$ orientation. (f) is the local zone of (e), which shows the difference of the atomistic arrangement between variants I and II. The blue color represents the ideal bcc structure and the orange color represents the ideal hcp structure according to the visualization method by Ackland [27]. (For interpretation of the references to color in this figure legend, the reader is referred to the web version of this article.)

(Fig. 5d), we can see that more hcp nuclei (the (0001) planes of the nuclei are either parallel to the $(10\bar{1})_{\text{bcc}}$ basal plane or parallel to the $(101)_{\text{bcc}}$ basal plane) are generated from the distorted bcc regions and grow quickly. Finally, the whole system transforms to the hcp structure at 188.1 K (Fig. 5e). We note that the product of the MT (shown in Fig. 5e) contains four types of variants, including two hcp anti-variants with (0001) planes parallel to the $(10\bar{1})_{\text{bcc}}$ basal plane (variants I and II; their difference is shown in Fig. 5f) and another two hcp anti-variants with (0001) planes parallel to the $(101)_{\text{bcc}}$ basal planes (variants III and IV; their difference is the same as that between variants I and II). These results indicate that the increase in diffuse scattering along $[101]^*$ and $[10\bar{1}]^*$ at M_s will lead to four types of hcp variants after phase transformation.

For the cooling process, in which the diffuse scattering along the $[110]^*$ (Fig. 2e) and $[1\bar{1}0]^*$ or $[0\bar{1}1]^*$ (Fig. 2f) and $[011]^*$ directions survive at the transformation temperature, we find that the corresponding products of the MT also only include four types of variants. Therefore we can conclude that the enhanced diffuse scattering along one conjugate of the $\langle 110 \rangle^*$ direction (e.g. $[101]^*$ and $[10\bar{1}]^*$) can result in four types of hcp variants as the product of phase transformation. The above results also indicate that, for a bulk single crystal for which the size is much larger than the MD cell we used here, there should be 12 types of hcp variants after a temperature-induced bcc–hcp transformation.

For the $[100]$ uniaxial tensile/compressive stress-induced MT, our corresponding atomic evolution also showed that the enhanced diffuse scattering along one of the $\langle 110 \rangle^*$ conjugate directions can result in four types of hcp variants as the products of phase transformation. See [Supplementary Material](#) for the case in which diffuse scattering along the $[101]^*$ (the same case as in Fig. 4a–c) and $[10\bar{1}]^*$ directions are dominant under the critical stress. We can thus conclude that for a bulk single crystal there should be eight types of hcp variants after the $[100]$ uniaxial tensile stress-induced bcc–hcp transformation, while only four of the hcp variants can be obtained after the $[100]$ uniaxial compressive stress-induced MT.

4. Discussion

4.1. Relationship between diffuse scattering and the products of temperature-induced martensitic transformation

From the above results, we can clearly see that the difference in diffuse scattering prior to a temperature- and uniaxial stress-induced MT leads to different types of hcp variants after the phase transformation. It is then natural to question what the relationship is between the diffuse scattering prior to the MT and the MT products, and what are the underlying reasons for this relationship. In this section, we will show that it is the transformation mechanism that determines the possible transformation pathway, and then influences the possible diffuse scattering prior to the MT and the products after the MT.

It is generally realized that the mechanism of the bcc–hcp transformation is the so-called Burgers mechanism [21], which first established the crystallographic relationship between the bcc and hcp structures:

$$(110)_{\text{bcc}} \parallel (0001)_{\text{hcp}} \text{ and } [\bar{1}11]_{\text{bcc}} \parallel [\bar{2}110]_{\text{hcp}}$$

The transformation can be achieved by the superposition of two coupled steps: (1) the displacement of neighboring (110) planes in the $[\bar{1}10]$ direction with an amplitude of $\frac{\sqrt{2}}{2}a$, where a is the lattice constant of the bcc structure. This displacement is needed to achieve the correct stacking sequence of the hcp structure and is referred to as a shuffle; and (2) two equivalent long wavelength distortions, such as $(1\bar{1}2)[\bar{1}11]$ and $(\bar{1}12)[1\bar{1}1]$, squeeze the angle from 70.53° to 60° in the basal plane; this is referred to as shear.

The bcc–hcp transformation is recognized as a shuffle-dominant phase transformation [28,29]. As shuffle occurs in $\{110\}\langle 1\bar{1}0 \rangle_{\text{bcc}}$ directions, there exist six crystallographically equivalent $\{110\}$ planes, and the shuffle directions in each plane can be completely opposite, e.g. the shuffle in the $(10\bar{1})$ plane can be along either the $[101]$ or the $[\bar{1}0\bar{1}]$ direction. In addition, according to the Burgers mechanism, each of the $\{110\}\langle 1\bar{1}0 \rangle_{\text{bcc}}$ shuffles will lead to one $(0001)_{\text{hcp}}$ variant after phase transformation. As a result, from the transformation mechanism, there should exist 12 equivalent shuffles in the bcc crystal, and these shuffles will lead to 12 equivalent hcp variants after the MT. Furthermore, as the diffuse scattering along the $\langle 110 \rangle^*$ directions prior to the MT arises from the atomic movements (or shuffle) in the $\{110\}$ planes prior to the MT, and $[110]^*$ represent the shuffles along both the $(1\bar{1}0)[110]$ and $(1\bar{1}0)[\bar{1}\bar{1}0]$ directions, there should exist six equivalent diffuse scattering streaks prior to the MT.

For a temperature-induced MT, due to the randomness of the thermal fluctuations, all 12 equivalent shuffles have the same probability of occurring, thus there should be an increase in diffuse scattering along six of the $\langle 110 \rangle^*$ directions prior to the MT that form 12 types of hcp variants after the MT.

We now explain the corresponding relationship between the diffuse scattering and martensitic variants after the temperature-induced MT. Here we use the $[101]^*$ and $[10\bar{1}]^*$ as an example. The $[101]^*$ and $[10\bar{1}]^*$ arise from the atomic movement (or shuffle) in the $(10\bar{1})$ and (101) planes respectively. For the shuffles in the $(10\bar{1})$ plane (red rectangle in Fig. 6), the atoms can shuffle with two opposite directions ($[101]$ and $[10\bar{1}]$), thus forming two $(0001)_{\text{hcp}}$ anti-variants (variants I and II in Fig. 6). The atoms can also shuffle in the conjugate (101) plane (light blue rectangle in Fig. 6) with two opposite directions ($[\bar{1}01]$ and $[10\bar{1}]$), and form another two $(0001)_{\text{hcp}}$ anti-variants (variants III and IV in Fig. 6), which are perpendicular to variants I and II. As a result, the projection of the four types of hcp variants to the $(10\bar{1})$ plane includes two $(0001)_{\text{hcp}}$ variants (projection of variants I and II) and two $(1100)_{\text{hcp}}$ variants (projection of variants III and

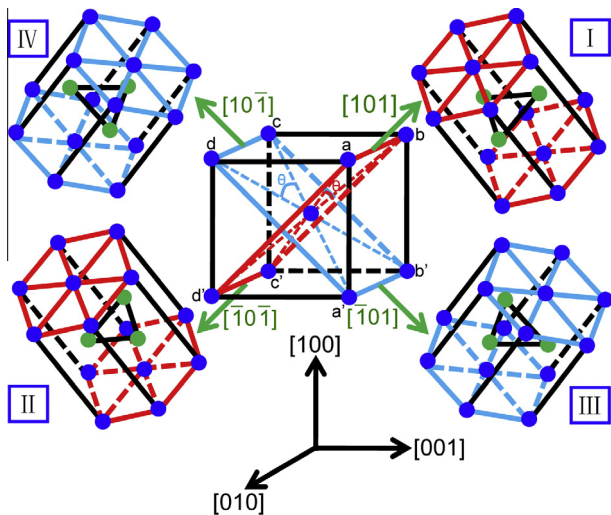


Fig. 6. The crystallographical relationship between the transformation mechanism and the product of martensite for the bcc–hcp phase transformation, indicating that the atoms can shuffle along two opposite directions in each $\{110\}$ basal plane, e.g. the $[101]$ and $[\bar{1}01]$ directions in the (101) plane (red color) or the $[10\bar{1}]$ and $[\bar{1}01]$ directions in the $(10\bar{1})$ plane (light blue color) (shown as green arrows in the figure), and form one pair of hcp anti-variants. One conjugate shuffle, e.g. the shuffles in the $(10\bar{1})$ (red color) and (101) (light blue color) planes (shown as rectangles in the middle cube), will lead to four types of hcp variants. (For interpretation of the references to color in this figure legend, the reader is referred to the web version of this article.)

IV). Thus two preferred transformation pathways with opposite shuffle directions lead to a single specific diffuse scattering streak prior to the MT and form one specific pair of anti-variants after the MT. This further indicates that the appearance of diffuse scattering streaks prior to the MT can act as an indicator for the preferred transformation pathways before the MT and the selection of martensitic variants after the MT.

Finally, to verify the above reasoning, we compared the present results with experiments. For the temperature-induced bcc to hcp phase transformation, the diffuse scattering intensity in $\text{Zr}_{0.985}\text{Co}_{0.015}$ and $\text{Zr}_{0.92}\text{Nb}_{0.08}$ was measured, and we observed that, at 1273 K, the diffuse scattering intensity is high along $[110]^*$ and $[1\bar{1}0]^*$ viewed from the $[001]$ zone axis [24], similar to the present work in Fig. 3. This indicates that, for a given phase transformation mechanism (the Burgers mechanism for bcc to hcp phase transformation), the diffuse scattering is the same and does not depend on the transformation temperature. Furthermore, prior to the B2–R phase transformation in TiNiFe alloys [10–14] and the B2–O/DO₁₉ phase transformation in Ti–22Al–27Nb alloy [26], the transformation mechanism requires a shuffle along $\{110\}\langle 1\bar{1}0\rangle_{\text{b2}}$. It [10–14,26] has also been observed that the existence of diffuse scattering along three of the crystallographically equivalent $(110)^*$ directions ($[110]^*$, $[101]^*$ and $[0\bar{1}1]^*$ directions), viewed from the $[1\bar{1}\bar{1}]$ zone axis, is similar to the present Fig. 2a–c. This comparison further confirms that it is the transformation mechanism that determines the possible transformation pathways, and then influences the possible

diffuse scattering prior to the MT and the products after the MT. This is valid not only in the generic bcc to hcp phase transformation, but also for other types of martensitic transformation.

4.2. Effect of external stress on the transformation pathways and the diffuse scattering prior to phase transformation

We have noted the differences between the diffuse scattering phenomena prior to temperature- and uniaxial tensile/compressive stress-induced MTs. However, the reasons for the difference in the diffuse scattering prior to uniaxial tensile stress- and compressive stress-induced MT are not clear. Considering the Burgers mechanism and crystallography, we find that the applied stress can change the shear order parameter of the phase transformation, and subsequently determines the preferred transformation pathways and the distribution of diffuse scattering streaks.

As discussed above, the shear on the $(1\bar{1}2)[\bar{1}11]$ and $(\bar{1}12)[1\bar{1}1]$ planes/directions squeezes the shear angle θ from 70.53° to 60° in the basal plane ($\{110\}_{\text{bcc}}$). For the bcc parent phase, the initial value of θ (shown in Fig. 6) in all six equivalent $\{110\}$ planes are the same. However, the presence of the external stress will force the ideal bcc box into a distorted bcc box, and thus change the shear angle in the $\{110\}_{\text{bcc}}$ basal planes. Fig. 7a shows the effect of $[100]$ uniaxial tension on the bcc unit cell. Clearly, the $[100]$ uniaxial tension causes shrinkage in the $[010]$ and $[001]$ directions, thus leading to the shear angles in the (110) , $(1\bar{1}0)$, (101) and $(10\bar{1})$ planes (blue rectangle) to be smaller than the undistorted one (black rectangle), and the shear angles in the (011) and $(0\bar{1}1)$ planes (red rectangle) to be larger than 70.53° . Fig. 7b shows that the $[100]$ uniaxial compression leads to the shear angles in the (110) , $(1\bar{1}0)$, (101) and $(10\bar{1})$ planes (red rectangle) being larger than 70.53° , whereas the shear angles in the (011) and $(0\bar{1}1)$ planes (blue rectangle) are smaller than 70.53° . Thus, we can conclude that the external field has a direct effect on the shear order parameter of the bcc–hcp phase transformation, and the effects of $[100]$ uniaxial tension are totally opposite to those of $[100]$ uniaxial compression.

How does the change in shear order parameter subsequently influence the transformation pathways and the distribution of diffuse scattering prior to the MT? In the following we try to address this question by checking the atomic movements in the $\{110\}$ planes. In Fig. 7 the red and green atoms on the $\{110\}$ planes represent the atoms in adjacent layers, the red arrows indicate the shuffle directions and the green arrows indicate the shear directions. We can clearly observe that the shear directions are totally opposite for the blue rectangles and red rectangles. Meanwhile, the movement of atom V in the rectangle is directly influenced by the atoms surrounding it in the adjacent layer (atoms I, II, III and IV). For the case where the shear angle θ decreases (blue rectangles in Fig. 7, e.g. (110) , $(1\bar{1}0)$, (101) and $(10\bar{1})$ planes under $[100]$ uniaxial tension,

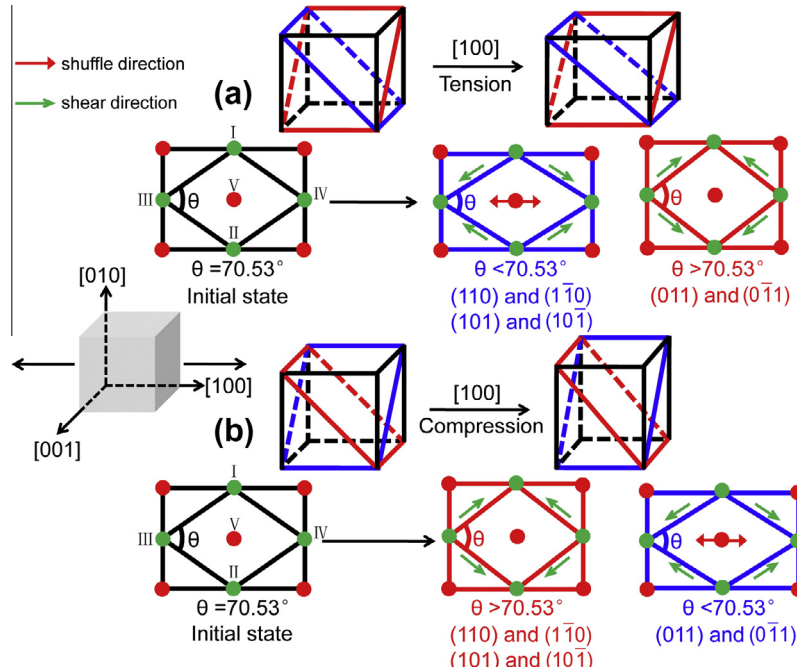


Fig. 7. Effect of uniaxial stress on the transformation mechanism for the bcc-hcp transformation showing that the applied stress changes the shear order parameter and thus influences the pathway of phase transformation. (a) [100] uniaxial tensile stress-induced martensitic transformation; (b) [100] uniaxial compressive stress-induced martensitic transformation. The blue rectangle represents the deformation in the (110), (1 $\bar{1}$ 0), (101) and (10 $\bar{1}$) planes under [100] uniaxial tension (a) and the (011) and (0 $\bar{1}$ 1) planes under [100] uniaxial compression (b); the red rectangle represents the deformation in the (011) and (0 $\bar{1}$ 1) planes under [100] uniaxial tension (a) and the (110), (1 $\bar{1}$ 0), (101) and (10 $\bar{1}$) planes under uniaxial compression (b). The red and green atoms represent the atoms in adjacent {110} plane layers, the red arrows indicate the shuffle directions and the green arrows indicate the shear directions. The shear directions are totally opposite in the blue and red rectangles (green arrows). (For interpretation of the references to color in this figure legend, the reader is referred to the web version of this article.)

(011) and (0 $\bar{1}$ 1) planes under [100] uniaxial compression), the shear decreases the distance between atoms I and II whereas it increases the distance between atoms III and IV. Due to the interactions with atoms I, II, III and IV, atom V is pushed away from its initial position towards one of the two opposite $\langle 1\bar{1}0 \rangle$ shuffle directions (shown as red arrows). The enhanced shuffles in these planes indicate that the bcc-hcp transformation in these planes is preferred, leading to an increase in diffuse scattering along the corresponding $\langle 110 \rangle^*$ directions (e.g. $[110]^*$, $[1\bar{1}0]^*$, $[101]^*$ and $[10\bar{1}]^*$ under [100] uniaxial tension, $[0\bar{1}1]^*$ and $[011]^*$ under [100] uniaxial compression) being observed prior to the MT. On the other hand, for the case that the shear angle θ increases (red rectangles in Fig. 7, e.g. (110), (1 $\bar{1}$ 0), (101) and (10 $\bar{1}$) planes under [100] uniaxial compression, (011) and (0 $\bar{1}$ 1) planes under [100] uniaxial tension), the shear increases the distance between atoms I and II but decreases the distance between atoms III and IV. As a result, atom V tends to move along the $\langle 100 \rangle$ direction but has difficulty in moving along the $\langle 1\bar{1}0 \rangle$ shuffle directions. Thus, the phase transformation pathways in these planes are not preferred, and the corresponding diffuse scattering (e.g. $[110]^*$, $[1\bar{1}0]^*$, $[101]^*$ and $[10\bar{1}]^*$ under [100] uniaxial compression, $[0\bar{1}1]^*$ and $[011]^*$ under [100] uniaxial tension) becomes weaker prior to the MT.

Based on the above understanding, we can further explain why diffuse scattering along the $[101]^*$ and $[10\bar{1}]^*$, $[110]^*$ and $[1\bar{1}0]^*$, and $[0\bar{1}1]^*$ and $[011]^*$ directions

are conjugate in the temperature- and [100] uniaxial stress-induced MTs. Here we still use $[101]^*$ and $[10\bar{1}]^*$ as an example. The shears on the (121)[111] and (121)[1 $\bar{1}$ 1] planes/directions squeeze the angle θ from 70.53° to 60° in the (10 $\bar{1}$)_{bcc} basal plane, and lead to the shrinkage of lines ab and $c'd'$ in Fig. 6. On the other hand, the shear on the (1 $\bar{2}$ 1)[111] and (1 $\bar{2}$ 1)[1 $\bar{1}$ 1] planes/directions leads to the shrinkage of lines $d'b'$ and cd in Fig. 6. As $ab = a'b' = cd = c'd'$ in a bcc crystal prior to the temperature-induced MT, the effect of shears on (121)[111] and (121)[1 $\bar{1}$ 1] is equivalent to the effect of shears on (1 $\bar{2}$ 1)[111] and (1 $\bar{2}$ 1)[1 $\bar{1}$ 1]. As the shears on (121)[111] and (121)[1 $\bar{1}$ 1] and on (1 $\bar{2}$ 1)[111] and (1 $\bar{2}$ 1)[1 $\bar{1}$ 1] help the shuffles in the (10 $\bar{1}$) and (101) planes, respectively (as discussed above), the shuffles in the (10 $\bar{1}$) and (101) planes are conjugate prior to the temperature-induced MT. Furthermore, prior to [100] tensile/compressive stress-induced MTs, $ab = a'b' = cd = c'd'$ is still valid in the distorted bcc box, thus the shuffles in the (10 $\bar{1}$) and (101) planes are still conjugate. As a result, we can observe conjugated diffuse scattering along the $[101]^*$ and $[10\bar{1}]^*$ directions prior to both the temperature- and [100] uniaxial stress-induced MTs.

In addition, we note that the [100] uniaxial stress is actually a high symmetric stress, which leads to equivalent deformation in the {110} planes (e.g. (110) and (1 $\bar{1}$ 0); (101) and (10 $\bar{1}$); (011) and (0 $\bar{1}$ 1)). As a result, we can see some conjugate diffuse scattering under [100] uniaxial

stress, e.g. $[0\bar{1}1]^*$ and $[01\bar{1}]^*$, $[110]^*$ and $[1\bar{1}0]^*$, and $[101]^*$ and $[1\bar{0}1]^*$. In a complex stress condition, the equivalence of deformation in $\{110\}$ planes may not hold, and there will no longer be conjugate diffuse scattering prior to the MT. However, the external field still needs to couple with the shear order parameter, and subsequently determines the preferred transformation pathways. It also has a bearing on the preferred diffuse scattering prior to the stress-induced MT and the products after the stress-induced MT.

The present work may also be useful in understanding the appearance of asymmetry in diffuse scattering intensity of the parent phase in the vicinity of the martensite starting temperature, as observed experimentally in $\text{Ni}_{51}\text{Fe}_{22}\text{Ga}_{27}$ and Ni–Mn–Ga systems [30,31]. It seems that, when close to M_s , the heterophase fluctuation gradually slows down and only one martensite nanodomain dominates the competition among all equivalent variants, eventually developing into a particular martensite variant. However, this selection is not preset and is highly sensitive to local and long-range fields.

5. Conclusions

We have used MD simulations to investigate the relationship between the transformation pathways, the diffuse scattering phenomena prior to martensitic transformations and product variants after transformation. The following conclusions are drawn.

- (1) The increase in diffuse scattering intensity also exists prior to a stress-induced martensitic transformation. However, unlike the diffuse scattering intensity prior to a temperature-induced MT, that prior to a stress-induced MT is closely related to the applied external fields.
- (2) The distribution of diffuse scattering can act as an indicator for the selection of martensitic variants, as there is a relationship between the transformation pathways, the diffuse scattering streaks prior to the MT and the products after the MT. For a bcc–hcp phase transformation, two preferred transformation pathways with opposite shuffle directions lead to a single specific diffuse scattering streak prior to the MT and form one pair of anti-variants after the MT.
- (3) The interaction between the transformation mechanism and the external field (e.g. temperature and stress) determines the preferred transformation pathways. In the bcc–hcp transformation, the external field can change the shear order parameter of the phase transformation, then determines the preferred transformation pathways and the distributions of diffuse scattering prior to the MT.

Acknowledgements

We are grateful to the Natural Science Foundation of China (51171140, 51231008, 51320105014 and 51321003),

the National Basic Research program of China (2010CB631003, 2012CB619402 and 2012CB619401) and the Program of Introducing Talents of Discipline to Universities in China project (B06025) for their support. X.D., T.L. and A.S. thank the US Department of Energy at Los Alamos National Laboratory under grant (DE-AC52-06NA25396).

Appendix A. Supplementary material

Supplementary data associated with this article can be found, in the online version, at <http://dx.doi.org/10.1016/j.actamat.2013.11.068>.

References

- [1] Barsch GR, Krumhansl JA. Metall Trans A 1988;19:761.
- [2] Otsuka K, Ren X. Prog Mater Sci 2005;50:511.
- [3] Planes A, Manosa L. Solid State Phys 2001;55:159.
- [4] Satija SK, Shapiro SM, Salamon MB, Wayman CM. Phys Rev B 1984;29:6031.
- [5] Shapiro SM, Yang BX, Noda Y, Tanner LE, Schryvers D. Phys Rev B 1991;44:9301.
- [6] Zheludev A, Shapiro SM, Wochner P, Schwartz A, Wall M, Tanner LE. Phys Rev B 1995;51:11310.
- [7] Stipcich M, Manosa L, Planes A, Morin M, Zarestky J, Lograsso T, et al. Phys Rev B 2004;70:054115.
- [8] Ren X, Miura N, Zhang J, Otsuka K, Tanaka K, Koiwa M, et al. Mater Sci Eng A 2001;312:196.
- [9] Manosa L, Jurado M, Planes A, Zarestky J, Lograsso T, Stassis C. Phys Rev B 1994;49:9969.
- [10] Shindo D, Murakami Y, Ohba T. MRS Bull 2002;27:121.
- [11] Murakami Y, Shindo D. Philos Mag Lett 2001;81:631.
- [12] Murakami Y, Shibuya H, Shindo D. J Microsc 2001;203:22.
- [13] Shindo D, Murakami Y. Sci Technol Adv Mater 2000;1:117.
- [14] Cai W, Murakami Y, Otsuka K. Mater Sci Eng A 1999;273:186.
- [15] Schryvers D, Tanner LE. Ultramicroscopy 1990;32:241.
- [16] Ding X, Zhang J, Wang Y, Zhou Y, Suzuki T, Sun J, et al. Phys Rev B 2008;77:174103.
- [17] Ding X, Suzuki T, Ren X, Sun J, Otsuka K. Phys Rev B 2006;74:104111.
- [18] Ding X, Suzuki T, Sun J, Ren X, Otsuka K. Mater Sci Eng A 2006;438:113.
- [19] Mendelev MI, Ackland GJ. Philos Mag Lett 2007;87:349.
- [20] Kaufmann AR, Magel TT. In: Lustman B, Kerze F, editors. Metallurgy of zirconium. New York: McGraw-Hill; 1955.
- [21] Burgers WG. Physica (Amsterdam) 1934;1:561.
- [22] Plimpton S. J Comput Phys 1995;117:1.
- [23] Li J. Model Simulat Mater Sci Eng 2003;11:173.
- [24] Heimann A, Petry W, Vogl G, Trampenau J, Schober HR, Chevrier J, et al. Z Phys B 1991;85:239.
- [25] Becquart CS, Clapp PC, Rifkin JA. Phys Rev B 1993;48:1.
- [26] Ren X, Hagiwara M. Acta Mater 2001;49:3971.
- [27] Ackland GJ, Jones AP. Phys Rev B 2006;73:054104.
- [28] Lindgård Per-Anker, Mouritsen Ole G. Phys Rev Lett 1986;57:19.
- [29] Sanati M, Saxena A, Lookman T, Albers RC. Phys Rev B 2001;63:224114.
- [30] Murakami Y, Shindo D, Kainuma R, Oikawa K, Ishida K. Appl Phys Lett 2008;92:102512.
- [31] Tsuchiya K, Tsutsumi A, Nakayama H, Ishida S, Ohtsuka H, Umemoto M. J Phys IV 2003;112:907.